Foreshock Seismicity Suggests Gradual Differential Stress Increase in the Months Prior to the 3 September 2016 M_w 5.8 Pawnee Earthquake

by Jacob I. Walter, Jefferson C. Chang, and Peter J. Dotray

ABSTRACT

The 3 September 2016 M_w 5.8 Pawnee earthquake was the largest earthquake in Oklahoma history. To determine the relationship with nearby seismic activity and whether there were any precursory foreshocks to the event, we analyze a dataset comprising regional seismometers throughout Oklahoma, including the Oklahoma Geological Survey statewide network. We use a matched-filter technique to identify potential missing earthquakes before and after the mainshock. This technique utilizes cataloged waveforms as templates that, when correlated against continuous waveforms, are able to identify repeating or nearby earthquakes. As shown in other studies, the aftershocks roughly fall along an east-southeast-trending linear belt that illuminates a previously unknown fault. We utilize the augmented seismicity catalog to draw two main conclusions. From standard statistical seismological methods, we deduce that the *b*-value decreased prior to the Pawnee mainshock; previous work suggests that *b*-value and differential stress are anticorrelated. The *b*-value result suggests the differential stress along the fault that eventually ruptured was gradually increasing in the few months leading up to the mainshock. During the aftershock period, we infer an Omori–Utsu *p*-value close to 1, typical for most tectonic events. Although the prolonged seismicity in the months leading up to the event may be a hallmark of induced earthquakes and may help decipher induced earthquakes from natural earthquakes, the rate of aftershocks is indistinguishable from natural tectonic earthquakes though deficient in larger aftershocks.

Electronic Supplement: Frequency–magnitude plot, *b*-value plots, and plot of cumulative earthquakes and cumulative seismic moment for matched-filter earthquake catalogs.

INTRODUCTION

The 3 September 2016 M_w 5.8 Pawnee earthquake is, so far, the largest recorded earthquake in Oklahoma history. Since early 2010, the central United States has experienced an unprecedented increase in seismicity widely believed to be induced (Ellsworth, 2013). The increasing trend of midcontinent seismicity is largely driven by substantial amounts of Oklahoma-felt seismicity since 2010, including the November 2011 M_w 5.7 Prague earthquake (Keranen *et al.*, 2013), the February 2016 M_w 5.1 Fairview earthquake (Yeck, Weingarten, *et al.*, 2016), the September 2016 M_w 5.8 Pawnee earthquake (Yeck, Hayes, *et al.*, 2016; X. Chen *et al.*, unpublished manuscript, 2017; see Data and Resources), and the November 2016 M_w 5.0 Cushing earthquake. The increase in earthquake activity in Oklahoma has been approximately concurrent with the widespread adoption of the horizontal drilling and industry activity in the Mississippi Lime, which produces significant formation water. This has led to a large-scale increase in produced water injected directly into the Arbuckle Group, a karstic aquifer directly overlying the basement rocks throughout most of Oklahoma (Murray, 2015).

Regional trends indicate some spatial and temporal links between high-volume injection wells and earthquakes (Weingarten *et al.*, 2015), including a correlation between disposed formation-produced water and seismicity in Oklahoma (Walsh and Zoback, 2015). Subsequent studies utilizing nearby temporary and rapid seismic network deployments have bolstered the link between wastewater injection and earthquakes along various fault strands throughout Oklahoma (Keranen *et al.*, 2013; McNamara *et al.*, 2015). Recent studies suggest that limiting factors controlling the size of induced earthquakes are the geometry of critically stressed faults (Yeck, Weingarten, *et al.*, 2016) and whether the pre-existing faults have favorable fault orientations (Holland, 2013; Walsh and Zoback, 2016).

Seismicity may be the best indicator of the current stress state of fault zones, and extrapolating frequency–magnitude relationships of small seismic sequences may allow us to understand the frequency of occurrence for the rare and larger events. The power-law distribution of earthquakes of a given magnitude is commonly referred to as the Gutenberg–Richter law (Ishimoto and Iida, 1939; Gutenberg and Richter, 1944), such that

$$\mathrm{Log}_{10}N = a - bM,$$

doi: 10.1785/0220170007

in which N is the cumulative number of earthquakes above **M** magnitude, a is the intercept, and b is the slope of the line fit to the data. Globally and over a long duration of observation, b-value tends to be ~1 (Frohlich and Davis, 1993), though numerous studies show b-values can vary spatially for different regions and tectonic settings, even along the same fault. One promising avenue for understanding spatial and temporal variations in b-value is the potential to understand fault-zone stress state and realistically constrain potential future earthquake rupture areas. An example was the 2012 Nicoya Peninsula earthquake, which nucleated in the same small region that a previous study inferred to have a low b-value (Ghosh *et al.*, 2008; Protti *et al.*, 2014; Walter *et al.*, 2015).

Although spatial patterns may emerge, b-value temporal variations are controversial, in part due to the inherent problem of statistics with small numbers and biases introduced using local catalogs. Nonetheless, a number of studies suggest that b-value may decrease prior to large earthquakes, such as the 2004 Sumatra earthquake (Nuannin *et al.*, 2005) or the 2011 Tohoku earthquake (Nanjo *et al.*, 2012). At the microscale, evidence also suggests a temporal decrease in b-value prior to slip for laboratory-generated earthquakes (Goebel *et al.*, 2013). In all these case studies, the b-value tends to decrease prior to the mainshock. Variations in stress along the same fault systems where rupture eventually nucleates (Schorlemmer and Wiemer, 2005), in addition to variations in b-value across different stress regimes (Schorlemmer *et al.*, 2005), all suggest a potential relationship in which differential stress is inversely proportional to b-value.

We use a case study of the 3 September 2016 Pawnee earthquake to better understand the role of small-scale seismicity during the foreshock and aftershock periods. The Oklahoma Geological Survey performs routine earthquake detection and location of earthquakes throughout the state, utilizing their and other agencies' permanent and temporary seismometers. In the years prior to the Pawnee earthquake, there was substantial activity in the vicinity of the system of faults directly near the Pawnee mainshock (Fig. 1), and there is some evidence of foreshock activity on an intersecting fault strand to the north of the unmapped fault that ruptured during the Pawnee earthquake (X. Chen *et al.*, unpublished manuscript, 2017; see Data and Resources; Fig. 1). Because the closest station to the earthquake was greater than 30 km away (QUOK) and there was a relatively sparse network at the time, we utilize a regional network matched-filter technique (Meng *et al.*, 2012) to build an earthquake catalog to test whether there was a systematic decrease in the b-value leading up to the mainshock. In addition, we analyze the aftershock period to determine whether any distinguishing patterns emerge for the Pawnee mainshock–aftershock sequence that may indicate it behaved in a way distinct from natural tectonic earthquakes.

DATA AND METHODS

As in other studies (e.g., Frohlich *et al.*, 2015; Walter *et al.*, 2016), we downloaded regional seismic data from 27 stations throughout Oklahoma; specifically from stations that have been installed for longer than a year. We avoid temporary networks so that the high concentration of stations over a small area, which would be the case with temporary networks in Oklahoma at the time, does not bias the regional detection or relocation of earthquakes specifically near the Pawnee rupture area. Rather than relying on short-term average/long-term average triggers or other methods for detecting aftershocks, we manually picked aftershocks using Antelope's *dbpick* waveform viewer and performed an initial location with *dbloc2*, utilizing a local tomographic 1D velocity model from a previous study (Keranen *et al.*, 2013). Then, we relocated events using a double-difference algorithm, hypoDD (Waldhauser and Ellsworth, 2000).

Based on prior experience with regional network cross correlation (Walter *et al.*, 2016), we band-pass filtered the templates between 4 and 10 Hz, cut the waveforms 1 s before and 10 s after the phase arrival (P or S), and resampled the data at a 20-Hz uniform sample rate. The matched-filter technique computes the normalized cross-correlation coefficient (coefficient between −1 and 1) at each sample point for each individual template through each component. Then, we shift each of the normalized cross-correlation functions produced for the individual components, relative to the travel time of each component and stack. For a given template event, not all 27 stations may observe an arrival, hence we utilize only those phases picked by the analyst. In the case of S phases, because it is common practice for analysts to pick only one S-phase arrival on only one horizontal component, we use that S-phase arrival time for the other horizontal component, so that there are three components for detection, as long as the station observes an arrival. Detection occurs when any point within the stacked cross-correlation function exceeds at least 9 times the median absolute deviation (MAD) of the daily stack. We later evaluate seismicity catalogs for a range of MAD values.

Newly detected event magnitudes are commonly computed relative to the magnitude of the template event using the ratio between event amplitudes and assuming a logarithmic scaling between amplitude and magnitude (e.g., Meng *et al.*, 2012). However, this sometimes introduces errors to that magnitude computation because the new event is commonly lower amplitude or the new detection may consist of just a few stations with a large range of event amplitudes, resulting in a high standard error. To avoid this complication, we compute the magnitude directly from the seismograms of the newly detected event. We compute the Richter (local) magnitude using a calibrated attenuation–distance relationship (e.g., Walter *et al.*, 2016) tuned to Oklahoma.

To analyze temporal changes in seismicity, we maintain a window containing 120 events and slide the window by a one-quarter window length; the time length of each window may vary, but each data window contains 120 events. Within each window, we compute b-values on the matched-filter catalog using the maximum-likelihood method (Aki, 1965) including a correction for magnitude binning

$$b = \log_{10} e/(M_{\text{mean}} - (M_{\text{min}} - \Delta M/2))$$

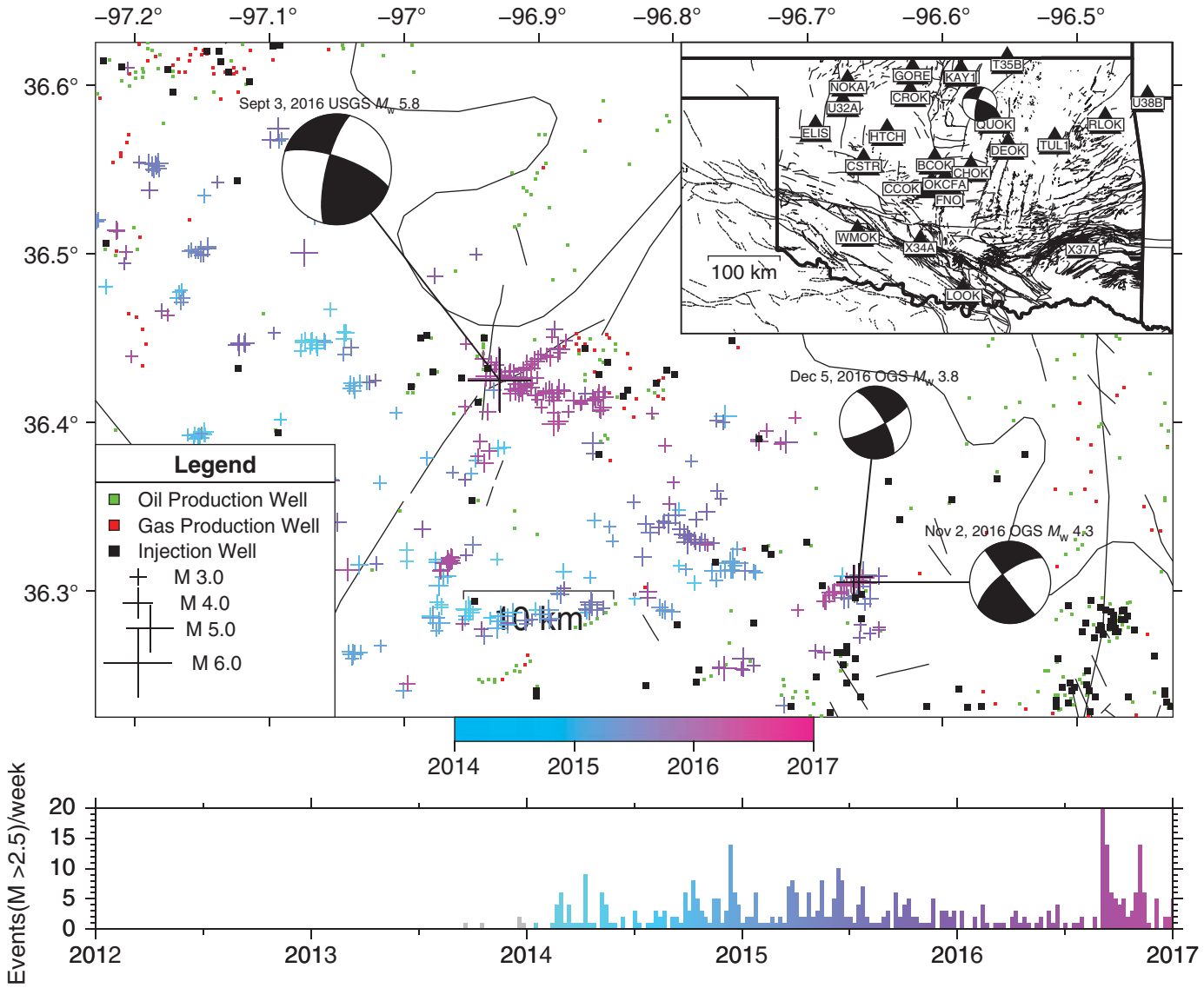

▲ **Figure 1.** U.S. Geological Survey (USGS) *W*-phase moment and location are plotted in black for the Pawnee earthquake and Oklahoma Geological Survey (OGS) determined focal mechanisms in black to the southeast. Mapped plus symbols are earthquakes (**M** >2.5) solely from the OGS catalog (see Data and Resources). Epicenters that appear in subsequent figures come from the matched-filter technique, which is wholly independent from the events shown in this figure. Straight black fault traces are from Holland (2015), and the arcuate black line indicates the county-line boundary separating Pawnee County to the south and Osage County to the north. Well locations, mapped as filled squares including oil (green), gas (red), and wastewater injection wells (black), are from Information Handling Services (IHS) datasets. (Inset) Map and station abbreviations for all stations utilized in the regional network waveform matched-filter analysis.

(Shi and Bolt, 1982), in which b is b-value, e is Euler's number, M_{mean} is the mean of all magnitudes in the window, M_{min} is the minimum magnitude in the window, and ΔM is the magnitude bin size (0.1). We compute the standard error σ_{sterr} of the b-value for the window of n earthquakes, in which $\sigma_{\text{sterr}} = b/\text{sqrt}(n)$; the greater number of earthquakes within a window reduces the error of the b-value estimation. We utilize the b-value to deduce whether any short-term changes in the b-value occur prior to the Pawnee mainshock.

During the aftershock period, the aftershock frequency often decays as an inverse power law and can be described by Omori–Utsu's formula

$$n(t) = K(t + c)^{-p},$$

in which n is the number of earthquakes as a function of time, t is the time since the mainshock, K and c are constants, and p is commonly referred to as the p-value and may be variable for different regions (Utsu, 1957). Utsu *et al.* (1995) evaluated many well-recorded aftershock sequences finding p-values that ranged from 0.6 to 2.5 with a median of 1.1 and observed no correlation between magnitude and p-value. We compute p-value and other Omori–Utsu parameters by computing the log-likelihood of the parameters and bootstrapping over 300 iterations (ZMAP software, Wiemer, 2001) and use a

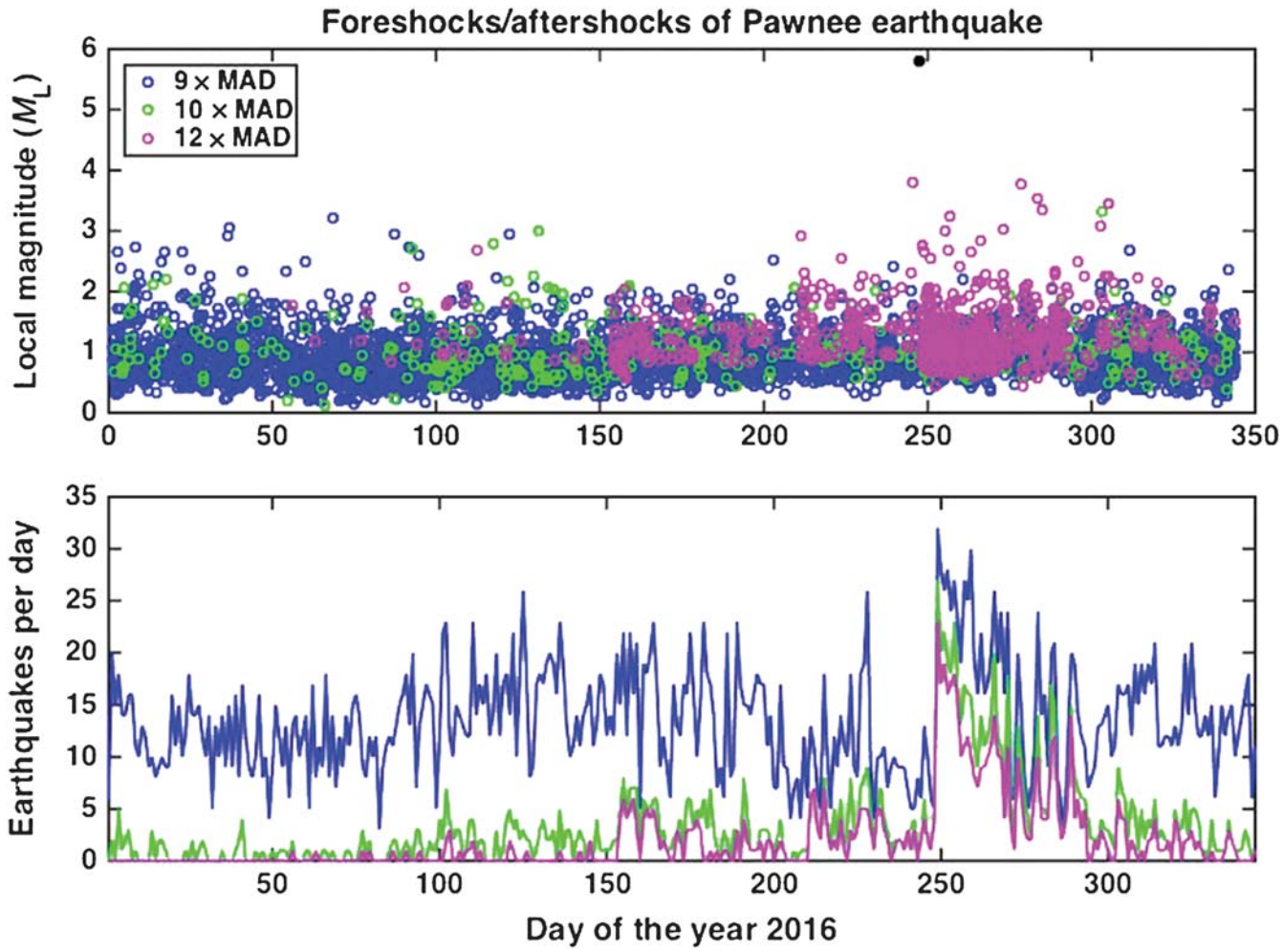

▲ **Figure 2.** (Top) Local magnitude for various median absolute deviation (MAD) thresholds during 2016. (Bottom) Seismicity rate for the same MAD thresholds over the same time period.

Kolmogorov–Smirnov test to determine if the fit of the data to the model is acceptable.

RESULTS AND DISCUSSION

We performed the matched-filter detection using 167 template events consisting of foreshocks and aftershocks in the area of the Pawnee earthquake (between 36.35°–36.5° N and 96.8°–97° W), manually identified by an analyst. We scanned through continuous waveforms from regional stations (Fig. 1, inset) between 1 January 2016 and 8 December 2016. With the network matched-filter detection, we find 2379 additional events with an MAD greater than 12. Within the immediate rupture area of the Pawnee earthquake (Fig. 2), we identify a total of 697 events that are 12 times the MAD (Fig. 2). Subsequently, lower thresholds of MAD values result in larger catalogs, but with lower MAD the chance of false detections increases. Based on previous experience, the MAD threshold can be widely variable, depending on the quality of the waveform data, the network geometry, and a host of other factors. In our experience with our technique and this dataset, to reduce the potential for false detections and maximize the number of detections, a value of 9 times the MAD is the minimum value.

We performed the hypoDD relocation of catalog events, as well as cross-correlating individual arrival phases to infer a more precise relocation. The large epicentral distances for some of the regional arrival phases leads to the foreshock/aftershock relocation results (Fig. 3) appearing more diffuse than from the seismicity catalog obtained by the Oklahoma Geological Survey (Fig. 1). Though in a general sense, many of the aftershocks and foreshocks align along a previously mapped fault (Fig. 3), a similar finding to other recent studies (Yeck, Hayes, *et al.*, 2016; X. Chen *et al.*, unpublished manuscript, 2017; see Data and Resources). Because of the diffuse nature of the relocation results (Fig. 3), we refrain from interpreting any seismicity spatiotemporal relationships but use this step to ensure that the seismicity we evaluate is actually from near the Pawnee earthquake fault rather than other nearby sources.

For calculating the *b*-value, we evaluate a variety of MADs and calculate *b*-value according to Aki's maximum-likelihood method and compute the standard error within each window (Aki, 1965). We utilized a magnitude of completeness (M_c) of

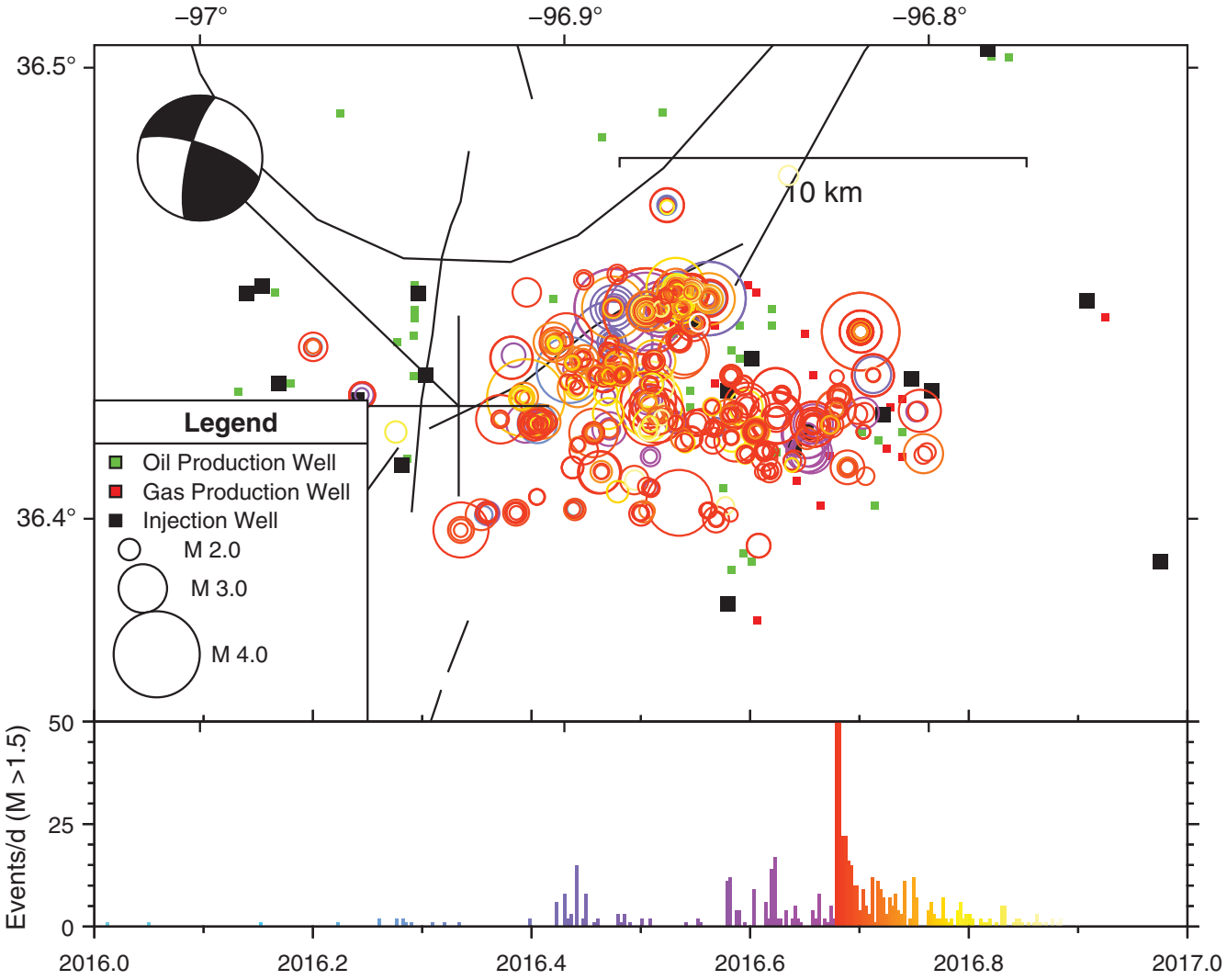

▲ **Figure 3.** HypoDD relocation of foreshocks and aftershocks. Foreshock seismicity indicates activity along a known fault, as well as the complementary unknown fault that eventually ruptured during the Pawnee mainshock. Events shown are a subset of the detected 9 times MAD catalog (M_L >1.5) with the lowest residuals (876 events). Black focal mechanism is the USGS-determined *W*-phase focal mechanism, and the plus sign maps to the point-source location of the mainshock (size of the plus symbol scales according to the mainshock magnitude).

1.5, which is a conservative estimate based on the data that suggest for events MAD > 9, the M_c is closer to 1 and approaching 1.5 for MAD > 12, Ⓔ Fig. S1). Although the matched-filter catalog suggests an M_c of 1.5, this completeness level relies on the small events produced by the technique; there is the potential that **M** > 1.5 events may go undetected if there is not a similar template event. We chose a moving window with a fixed number of events and in our analysis, the choice of window length was rather arbitrary, as shown in Ⓔ Figure S2, available in the electronic supplement to this article; almost all windows exhibited the same general trend. We show *b*-values with windows consisting of 120 events and slide by one-quarter window length for each iteration (Fig. 4). For all MAD threshold values, the data indicate a consistent trend of decreasing *b*-value right before the mainshock (same qualitative trend exhibited in Ⓔ Fig. S2). We verify one aspect of the *b*-value results by checking whether there was a rate dependence upon earthquake catalog completeness, in which events may be missed and alter the magnitude of completeness and *b*-value during periods of high-seismic activity. Utilizing a recently released algorithm (Hainzl, 2016), we found the high rate of earthquakes does not affect the magnitude of completeness during our study time period.

Figure 4 indicates some noticeable complexity to the *b*-value results, including the observation that shortly after the mainshock, the *b*-values increase significantly. The increase after the mainshock suggests a large number of smaller magnitude aftershocks occurring during the few weeks following the Pawnee mainshock. When we examine the results from the end of the study period, we find further complexity in which

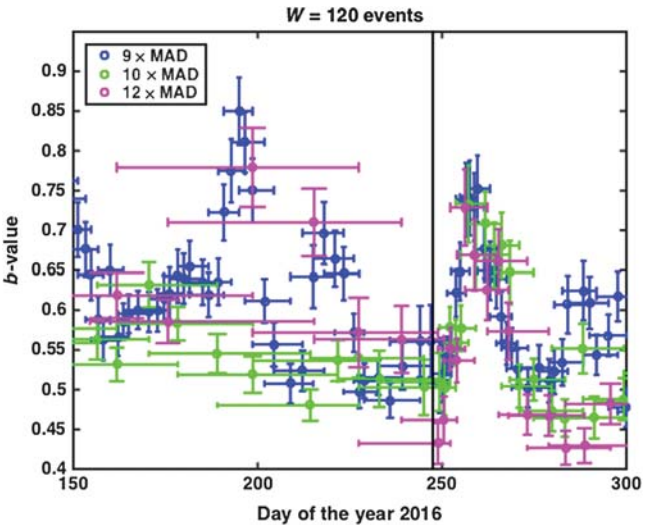

▲ **Figure 4.** *b*-value plots for the catalog at a range of MAD thresholds. Vertical error bars indicate standard error of the maximum-likelihood estimates, and horizontal error bars are the beginning and end of windows containing 120 events. The center of the window is plotted at the time corresponding to the timing of the center of the time window. The black vertical line is the timing of the Pawnee mainshock. All events analyzed correspond to those shown here and lie along the Pawnee mainshock previously unmapped fault or complementary mapped fault.

the *b*-values fall to lower values than observed prior to the mainshock. Other studies suggest that *b*-values are generally lower than 1 for areas under active injection for hydrocarbon (e.g., Huang and Beroza, 2015; Skoumal *et al.*, 2015), whereas slightly higher than 1 for areas near geothermal reservoirs (Shapiro *et al.*, 2011). One hypothesis would be that wastewater injection induces existing faults to slip, whereas geothermal stimulation creates disconnected cracks or microfaults that are less likely to nucleate larger events. Oklahoma wastewater injection has occurred in large volumes for a number of years, and the long-term fluctuations in *b*-values warrant further study in this region and others throughout the midcontinental United States.

Differential stresses that promote or retard earthquake slip are incredibly difficult to infer prior to moderate or large earthquakes. Even in Oklahoma, where the majority of earthquake activity suggests seismogenic depths are relatively shallow (4–8 km from the surface; Darold *et al.*, 2015), the stress state is difficult to infer by virtue of being a considerable distance from the surface. The small-scale seismicity and slope of the frequency–magnitude distribution (*b*-value) may indicate some temporal changes in the differential stress. The decreasing *b*-value suggests that the differential stress in the region may have been increasing during the months prior to the Pawnee earthquake. Overlapping windows and other issues with analyzing statistics of small datasets (made smaller by windowing) inhibit our confidence at estimating truly accurate estimates of *b*-value. For example, it is difficult to qualitatively observe any substantial decrease in the *b*-value estimates for the 12 times MAD dataset in Figure 3, because as the MAD threshold increases, the number of total events decreases, and the window with the fixed number of events increases, subsequently obscuring an otherwise visible decreasing trend. Nonetheless, in all cases the *b*-value appears to decrease in the months prior to the mainshock despite changes in MAD threshold. The result is yet another study added to the body of evidence suggesting that *b*-value decreases prior to stick-slip events in the laboratory (Goebel *et al.*, 2013) and prior to seismic events such as great earthquakes (Nuannin *et al.*, 2005; Nanjo *et al.*, 2012). This study suggests that moderate earthquakes may also exhibit a gradual *b*-value decrease prior to the moderate mainshock.

The first-order observation of prodigious precursory seismicity in the months leading up to the Pawnee earthquake may be a distinguishing feature of induced seismicity. One proposed hallmark for distinguishing between induced and natural events is establishing whether the induced sequence exhibits swarm-like behavior such as shown for a number of induced events or follows a more typical mainshock–aftershock behavior with large-magnitude events followed by smaller magnitude aftershocks (Skoumal *et al.*, 2015). During the prolonged precursory or foreshock period in the months leading up to the event, the Pawnee area exhibits swarm-like behavior (Fig. 2), including nearly constant low-magnitude events and no clear mainshock–aftershock sequences in the months leading up to the Pawnee mainshock.

We analyzed the aftershock period using our augmented seismicity catalog to infer aftershock productivity in the months after the Pawnee mainshock. Upon fitting the observed aftershock period to the Omori–Utsu model and using bootstrapping to determine the parameters of that equation, we find it is best fit with $p = 0.99$, $c = 5$, and $K = 153.8$ (Fig. 5). Utsu *et al.* (1995) analyzed more than 200 aftershock sequences and found a median value for p of 1.1. Thus, there is nothing to distinguish the Pawnee aftershock rate from a typical aftershock sequence, except for the lack of larger aftershocks (within a magnitude unit of the mainshock). This aligns with a recent study analyzing the frequency–magnitude relationships of many suspected induced earthquake sequences to determine if the statistical M_{max}, the extrapolation of frequency–magnitude distribution to larger magnitudes, for induced earthquakes might be different than for regular tectonic earthquakes (van der Elst *et al.*, 2016). That study concluded that there were no distinguishing factors with respect to the statistical M_{max} that separate natural and induced earthquakes. The Pawnee early aftershock rate is indistinguishable from that of a natural earthquake's aftershock rate, other than a lack of aftershocks of larger magnitude.

Determining whether the Pawnee earthquake was definitely induced by wastewater injection is beyond the scope of this article, but a nearby wastewater injection well suggests it is plausible, because a well within 7 km of the mainshock experienced a 50% increase in daily injection rate in the 3 months prior to the mainshock (Grandin *et al.*, 2017). Also, the occurrence of the mainshock amongst seismicity that essen-

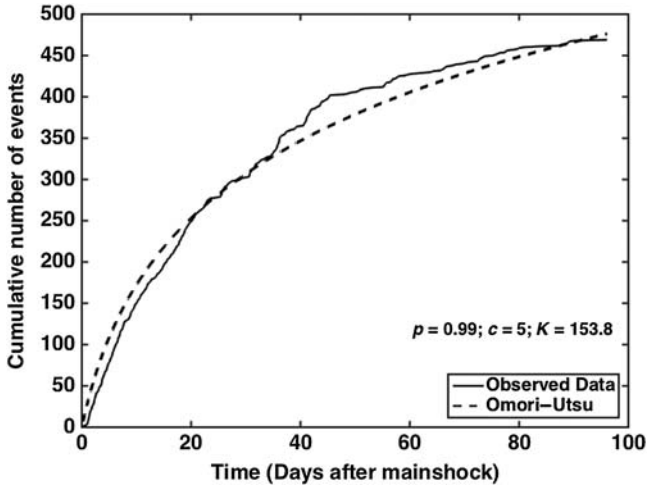

▲ **Figure 5.** Omori–Utsu fit to aftershock decay and Omori–Utsu parameters.

tially began in early 2014, when injection began in the area, suggests that it is more likely than not that the earthquake may have been induced by the culmination of injection activities, even if interearthquake interactions could have ultimately led to the more direct triggering of the mainshock (X. Chen *et al.*, unpublished manuscript, 2017; see Data and Resources). Whether the cascading effect of seismicity in the year prior may be a hallmark of induced seismicity is something that warrants further study.

CONCLUSION

Using aftershocks of the Pawnee earthquake, we performed a network matched-filter detection and detected an order-of-magnitude more earthquakes. We analyzed the earthquakes nearest to the Pawnee mainshock, and results suggest a decrease in *b*-value in the last few months prior to the Pawnee mainshock. If we examine the Pawnee earthquake solely with respect to the general characteristics of the seismicity, we find that the extended precursory period in the months prior to the Pawnee mainshock, at which the seismicity exhibits some swarm-like behavior, suggests that the Pawnee earthquake behavior is consistent with that of other induced earthquakes. The *p*-value we fit for the aftershock period suggests that the aftershock rate is not significantly different from the *p*-values determined for tectonic earthquakes, though Pawnee is deficient in larger magnitude aftershocks. This suggests that the first-order physics of induced earthquakes may be no different than that for tectonic earthquakes, once the earthquakes nucleate. Further study is needed to understand premainshock triggering of small earthquakes and interactions between small events that promote the large events to nucleate.

DATA AND RESOURCES

Seismic data utilized for this study came from the following seismic networks: OK (doi: 10.7914/SN/OK), N4 (doi: 10.7914/SN/N4), TA (doi: 10.7914/SN/TA), and US (doi: 10.7914/SN/US). Some of the figures were created using Generic Mapping Tools (Wessel *et al.*, 2013). Some analysis used the ZMAP tools (Wiemer, 2001). The matched-filter earthquake catalog is included as an Ⓔ electronic supplement to this article. The Oklahoma Geological Survey (OGS) catalog for the map and symbols for earthquakes shown in Figure 1 can be found at http://wichita.ogs.ou.edu/eq/catalog/complete/ (last accessed December 2016). The other information about the September 2016 M_w 5.8 Pawnee earthquake can be found at the unpublished manuscript by X. Chen, N. Nakata, C. Pennington, J. Haffener, J. Chang, X. He, Z. Zhan, S. Ni, and J. I. Walter (2017). The Pawnee earthquake as a result of the interplay among injection, tectonic faults and foreshocks.

ACKNOWLEDGMENTS

The authors wish to thank Rob Skoumal and an anonymous reviewer for constructive reviews that improved this article.

REFERENCES

Aki, K. (1965). Maximum likelihood estimate of *b* in the formula log $(N) = a - bM$ and its confidence limits, *Bull. Earthq. Res. Inst. Tokyo Univ.* **43,** 237–239.

Darold, A. P., A. A. Holland, J. K. Morris, and A. R. Gibson (2015). Oklahoma earthquake summary report 2014, *Okla. Geol. Surv. Open-File Rept. OF1-2015*, 46 pp.

Ellsworth, W. L. (2013). Injection-induced earthquakes, *Science* **341,** no. 6142, doi: 10.1126/science.1225942.

Frohlich, C., and S. D. Davis (1993). Teleseismic b values; or, much ado about 1.0, *J. Geophys. Res.* **98,** 631–644.

Frohlich, C., J. I. Walter, and J. F. W. Gale (2015). Analysis of transportable array (USArray) data shows earthquakes are scarce near injection wells in the Williston Basin, 2008–2011, *Seismol. Res. Lett.* **86,** 492–499.

Ghosh, A., A. V. Newman, A. M. Thomas, and G. T. Farmer (2008). Interface locking along the subduction megathrust from b-value mapping near Nicoya Peninsula, Costa Rica, *Geophys. Res. Lett.* **35,** L01301, doi: 10.1029/2007GL031617.

Goebel, T. H. W., D. Schorlemmer, T. W. Becker, G. Dresen, and C. G. Sammis (2013). Acoustic emissions document stress changes over many seismic cycles in stick-slip experiments, *Geophys. Res. Lett.* **40,** 2049–2054, doi: 10.1002/grl.50507.

Grandin, R., M. Vallee, and R. Lacassin (2017). Rupture process of the Oklahoma M_w 5.7 Pawnee earthquake from Sentinel-1 InSAR and seismological data, *Seismol. Res. Lett.* **88,** no. 4, doi: 10.1785/0220160226.

Gutenberg, B., and C. F. Richter (1944). Frequency of earthquakes in California, *Bull. Seismol. Soc. Am.* **34,** 185–188.

Hainzl, S. (2016). Rate-dependent incompleteness of earthquake catalogs, *Seismol. Res. Lett.* **87,** no. 2A, 337–344.

Holland, A. A. (2013). Optimal fault orientations within Oklahoma, *Seismol. Res. Lett.* **84,** no. 5, 876–890.

Holland, A. A. (2015). Preliminary fault map of Oklahoma, *Okla. Geol. Surv. Open-File Rept. OF3-2015*.

Huang, Y., and G. C. Beroza (2015). Temporal variation in the magnitude frequency distribution during the Guy-Greenbrier earthquake sequence, *Geophys. Res. Lett.* **42,** 6639–6646, doi: 10.1002/2015GL065170.

Ishimoto, M., and K. Iida (1939). Observations of earthquakes registered with the microseismograph constructed recently, *Bull. Earthq. Res. Inst.* **17,** 443–478.

Keranen, K. M., H. M. Savage, G. A. Abers, and E. S. Cochran (2013). Potentially induced earthquakes in Oklahoma, USA: Links between wastewater injection and the 2011 M_w 5.7 earthquake sequence, *Geology* **41,** doi: 10.1130/G34045.1.

McNamara, D. E., H. M. Benz, R. B. Herrmann, E. A. Bergman, P. Earle, A. Holland, R. Baldwin, and A. Gassner (2015). Earthquake hypocenters and focal mechanisms in central Oklahoma reveal a complex system of reactivated subsurface strike-slip faulting, *Geophys. Res. Lett.* **42,** 2742–2749, doi: 10.1002/2014GL062730.

Meng, X., X. Yu, Z. Peng, and B. Hong (2012). Detecting earthquakes around Salton Sea following the 2010 M_w 7.2 El Mayor-Cucapah earthquake using GPU parallel computing, *Procedia Comput. Sci.* **9,** 937–946, doi: 10.1016/j.procs.2012.04.100.

Murray, K. E. (2015). Class II saltwater disposal for 2009–2014 at the annual-, state-, and county-scales by Geologic Zones of Completion, Oklahoma, *Okla. Geol. Surv. Open-File Rept. OF5-2015*, 18 pp., Norman, Oklahoma.

Nanjo, K. Z., N. Hirata, K. Obara, and K. Kasahara (2012). Decade-scale decrease in b value prior to the M 9-class 2011 Tohoku and 2004 Sumatra quakes, *Geophys. Res. Lett.* **39,** L20304, doi: 10.1029/2012GL052997.

Nuannin, P., O. Kulhanek, and L. Persson (2005). Spatial and temporal b value anomalies preceding the devastating off coast of NW Sumatra earthquake of December 26, 2004, *Geophys. Res. Lett.* **32,** L11307, doi: 10.1029/2005GL022679.

Protti, M., V. Gonzalez, A. V. Newman, T. H. Dixon, S. Y. Schwartz, J. S. Marshall, L. Feng, J. I. Walter, R. Malservisi, and S. E. Owen (2014). Nicoya earthquake rupture anticipated by geodetic measurement of the locked plate interface, *Nature Geosci.* **7,** 117–121, doi: 10.1038/ngeo2038.

Schorlemmer, D., and S. Wiemer (2005). Microseismicity data forecast rupture area, *Nature* **434,** 1086, doi: 10.1038/4341086a.

Schorlemmer, D., S. Wiemer, and M. Wyss (2005). Variation in earthquake-size distribution across different stress regimes, *Nature* **437,** 539–542, doi: 10.1038/nature04094.

Shapiro, S. A., O. S. Kruger, C. Dinske, and C. Langenbruch (2011). Magnitudes of induced earthquakes and geometric scales of fluid-stimulated rock volumes, *Geophysics* **76,** WC55–WC63, doi: 10.1190/GEO2010-0349.1.

Shi, Y., and B. A. Bolt (1982). The standard error of the magnitude-frequency b value, *Bull. Seismol. Soc. Am.* **72,** 1677–1687.

Skoumal, R. J., M. R. Brudzinski, and B. S. Currie (2015). Distinguishing induced seismicity from natural seismicity in Ohio: Demonstrating the utility of waveform template matching, *J. Geophys. Res.* **120,** doi: 10.1002/2015JB012265.

Utsu, T. (1957). Magnitude of earthquakes and occurrence of their aftershocks, *Zisin* **10,** 35–45.

Utsu, T., Y. Ogata, and R. S. Matsu'ura (1995). The centenary of the Omori formula for a decay law of aftershock activity, *J. Phys. Earth* **43,** 1–33.

van der Elst, N. J., M. T. Page, D. A. Weiser, T. H. W. Goebel, and S. M. Hosseini (2016). Induced earthquake magnitudes are as large as (statistically) expected, *J. Geophys. Res.* **121,** 4575–4590, doi: 10.1002/2016JB012818.

Waldhauser, F., and W. L. Ellsworth (2000). A double-difference earthquake location algorithm: Method and application to the northern Hayward fault, *Bull. Seismol. Soc. Am.* **90,** 1353–1368.

Walsh, F. R., and M. D. Zoback (2015). Oklahoma's recent earthquakes and saltwater disposal, *Sci. Adv.* **1,** e1500195, doi: 10.1126/sciadv.1500195.

Walsh, F. R., III, and M. D. Zoback (2016). Probabilistic assessment of potential fault slip related to injection-induced earthquakes: Application to north central Oklahoma, USA, *Geology* **44,** no. 12, doi: 10.1130/G38275.1.

Walter, J. I., P. J. Dotray, C. Frohlich, and J. F. W. Gale (2016). Earthquakes in northwest Louisiana and the Texas–Louisiana border possibly induced by energy resource activities within the Haynesville shale play, *Seismol. Res. Lett.* **87,** no. 2A, doi: 10.1785/0220150193.

Walter, J. I., Z. Peng, X. Meng, A. V. Newman, S. Y. Schwartz, and M. Protti (2015). Far-field triggering of foreshocks near the nucleation zone of the 5 September 2012 (M_w 7.6) Nicoya Peninsula, Costa Rica earthquake, *Earth Planet. Sci. Lett.* **431,** 75–86, doi: 10.1016/j.epsl.2015.09.017.

Weingarten, M., S. Ge, J. W. Godt, B. A. Bekins, and J. L. Rubinstein (2015). High-rate injection is associated with the increase in U.S. mid-continent seismicity, *Science* **348,** no. 6241, 1336–1340, doi: 10.1126/science.aab1345.

Wessel, P., W. H. F. Smith, R. Scharroo, J. Luis, and F. Wobbe (2013). Generic mapping tools: Improved version released, *Eos Trans. AGU* **94,** no. 45, 409–410.

Wiemer, S. (2001). A software package to analyze seismicity: ZMAP, *Seismol. Res. Lett.* **72,** 373–382.

Yeck, W. L., G. P. Hayes, D. E. McNamara, J. L. Rubinstein, W. D. Barnhart, P. S. Earle, and H. M. Benz (2016). Oklahoma experiences largest earthquake during ongoing regional wastewater injection hazard mitigation efforts, *Geophys. Res. Lett.* **43,** doi: 10.1002/2016GL071685.

Yeck, W. L., M. Weingarten, H. M. Benz, D. E. McNamara, E. A. Bergman, R. B. Herrmann, J. L. Rubinstein, and P. S. Earle (2016). Far-field pressurization likely caused one of the largest injection induced earthquakes by reactivating a large preexisting basement fault structure, *Geophys. Res. Lett.* **43,** 10,198–10,207, doi: 10.1002/2016GL070861.

Jacob I. Walter[1]
Jefferson C. Chang[2]
Oklahoma Geological Survey
University of Oklahoma
100 E. Boyd
Norman, Oklahoma 73019-0628 U.S.A.
jwalter@ou.edu

Peter J. Dotray
Institute for Geophysics
University of Texas at Austin
10100 Burnet Road, Building 196
Austin, Texas 78758 U.S.A.

Published Online 3 May 2017

[1] Also at the Institute for Geophysics, University of Texas at Austin, 10100 Burnet Road, Building 196, Austin, Texas 78758 U.S.A.

[2] Also at the ConocoPhillips School of Geology and Geophysics, University of Oklahoma, 100 E. Boyd Street, Norman, Oklahoma 73109 U.S.A.